International Forum on Aeroelasticity and Structural Dynamics
IFASD 2019
9-13 June 2019, Savannah, Georgia, USA

FLIGHT MECHANICAL DESIGN, FLIGHT DYNAMICS, AND FLIGHT CONTROL FOR MULTIBODY AIRCRAFT: A SUMMARY

Alexander Köthe[1]

[1]Technische Universität Berlin
Institute of Aeronautics and Astronautics
Flight Mechanics, Flight Control and Aeroelasticity
Marchstraße 12, 10587 Berlin, Germany
alexander.koethe@campus.tu-berlin.de

Keywords: Highly flexible aircraft, multibody dynamics, High-Altitude Pseudo Satellite (HAPS)

Abstract: Aircraft operating as so-called High-Altitude Platform Systems have been proposed to ba a complementary technology to satellites for several years. State-of-the-art HAPS solution have a high-aspect-ratio wing using lightweight construction. In gusty atmosphere, this results in high bending moments and high structural loads, which can lead to overloads. To overcome the shortcomings of such one-wing aircraft, so-called *multibody aircraft* have been considered to be an alternative. This aircraft technology has been investigated at TU Berlin's department of flight mechanics, flight control and aerolasticity (project "AlphaLink") in the last years. This paper presents a summary of the conducted research. After a review looking at the state of the art, the paper describes the design of an exemplary multibody aircraft. The designed reference model is capable of flying 365 days, for 24 hours, between the 40° north and south latitude with 450 kg payload operating in high altitudes with solar power only. Further, a complete flight dynamics model is provided and analyzed for aircraft that are mechanically connected at their wingtips. Using the non-linear flight dynamics model, flight controllers are designed to stabilize the plant and provide the aircraft with an eigenstructure similar to conventional aircraft. The resulting inner-control loops yield a multibody aircraft behavior that is similar to the one of a rigid aircraft. Hence, conventional outer-loops can be used for flight guidance.

1 INTRODUCTION

Today, satellites provide services that have a huge impact on society. Satellite networks like *Iridium* enable a truly global communication exchange between people all over the world [1]. Despite the advantages provided by their versatile applications, satellites are facing limitations in terms of operation and maintenance. Solar-powered High-Altitude Long-Endurance (HALE) aircraft are able to overcome these limitations. Since those aircraft may (at least partially) replace conventional satellites, the term High-Altitude Pseudo Satellites (HAPS) is being used [2]. HAPS have to be operated in the stratosphere for very long times. This requires a lightweight construction, high aerodynamic efficiency and the use of solar energy. At the time being, an endurance of nearly 624 hours is proven (cf. Airbus Zephyr S [3]). In addition, HAPS aircraft are not bound to a specific orbit. They can be operated in a certain region for a specific amount of time. After completing a mission, they can be recovered, relocated and used for another mission.

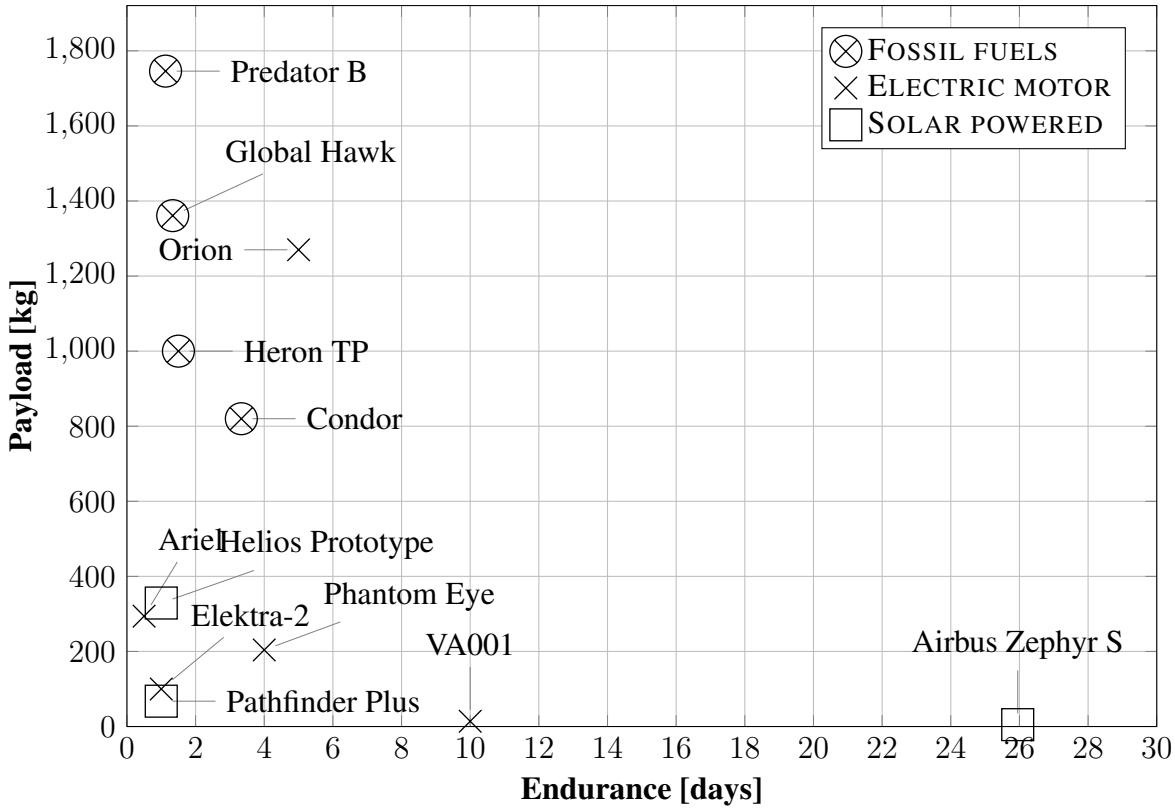

Figure 1: Payload and endurance for different unmanned aircraft (all already successfully flown), Sources: [4, 5]

An unmanned aircraft configuration suitable to replace satellites is not available yet. All HAPS aircraft share a common limitation: they either carry high payloads for a short time or substitute payload with fuel to operate to achieve a longer range. A sufficient combination of high payload and long endurance cannot be achieved at the moment. This indicates the empty top right area of the diagram in Fig. 1 (corresponding to long endurance with high payload). This is exactly the zone required for an unmanned aircraft technology that is capable of replacing satellite communication solutions.

A common shortcoming of current HAPS aircraft is their large wingspan. This can lead to large deformations with structural geometrical non-linearities since linear theory is only valid for small deformations. Due to a lacking consideration of those non-linearities, aircraft accidents like those observed with the NASA *Helios* in 2003 cannot be ruled out [6]. On the flight to mission altitude, the HAPS aircraft passes the troposphere, where most of the weather events occur, e.g. gusts or turbulence. Gusts may cause high aerodynamic loads leading to high bending moments, which ultimately can damage the structure. Additionally, non-uniform gust excitations of the highly flexible vehicle can occur, resulting in larger deformations than those caused by uniform ones [7]. Although Airbus Zephyr holds the current endurance world record, the payload capacity is very low and it is expected that payload increases will cause problems similar to those observed with other one-wing solutions. The main reason for the payload restriction is the high wing loading due to the combination of lightweight structure and large wingspan.

To overcome the shortcomings of such one-wing aircraft, so-called *multibody aircraft* are considered to be an alternative. The concept assumes multiple aircraft connected to each other at their wingtips. It goes back to the German engineer Dr. Richard Vogt. In the United States,

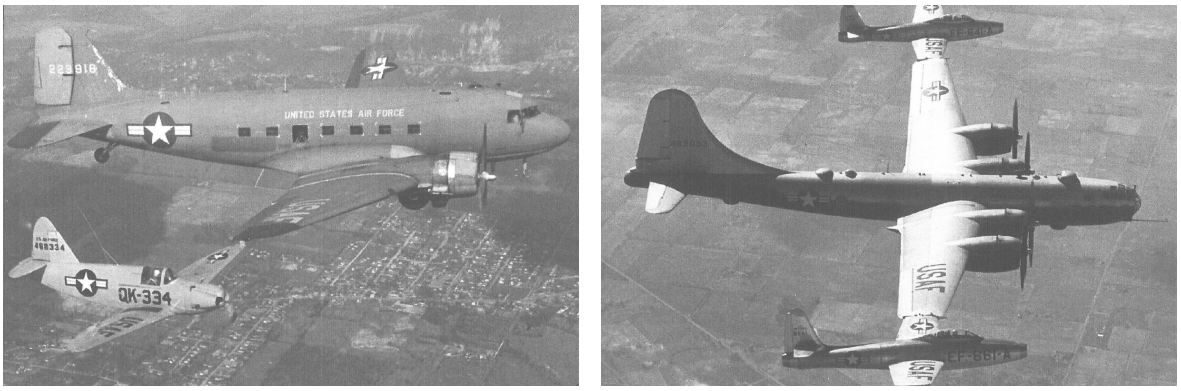

(a) Coupling of Culver Q-14 to a Douglas C-47 (b) Coupling of two Republic F-84D to a Boeing B-29

Figure 2: Wingtip-coupling experiments of the U.S. Air Force, source: [8]

shortly after the end of World War II, he experimented with the coupling of manned aircraft. This resulted in a high-aspect-ratio wing for the aircraft formation. The range of the formation could be increased correspondingly. The engineer Geoffrey S. Sommer took up Vogt's idea and patented an aircraft configuration consisting of several unmanned aerial vehicles coupled at their wingtips. However, the patent does not provide any insight into the flight performance, the flight mechanical modeling or the control of such an aircraft. Based on a state-of-the-art consideration of connected aircraft, TU Berlin's department of flight mechanics, flight control and aeroelasticity has addressed this knowledge gap within the internal project *AlphaLink* in the last years.

1.1 State of the Art

The German engineer Dr. Richard Vogt, who emigrated to the United States after World War II, proposed that extra floating panels carrying fuel tanks could be attached to wingtips with hinges in order to extend the effective wingspan of an aircraft. The effect would be a higher aspect ratio similar to a glider, a reduction of fuel consumption and, hence, a longer range. In the patent filed under US3,161,373, Vogt describes the method of coupling aircraft in spanwise direction to increase the lift-to-drag ratio without increasing the structural weight [9]. Vogt originated the wingtip-coupling configuration during World War II and the German Research Institute for Gliders conducted a preliminary evaluation in 1945 with light airplanes [8]. The hinge allowed the aircraft to roll, pitch and yaw with respect to each other. In 1949, a preliminary investigation was carried out in the United States. As shown in Fig. 2(a), a Culver Q-14 was successfully coupled to a Douglas C-47. In total, 230 tests were performed. After those tests, the so-called Tip Tow program was launched by coupling two Republic EF-84D Thunderjets to a Boeing EB-29A (cf. Fig. 2(b)). In terms of flight dynamics, problems occurred in roll control since the ailerons did not provide sufficient control authority. As the middle aircraft of the Tip Tow program had a straight wing, aircraft with swept wing were considered in subsequent studies, namely FICON (*Fighter Convoye*) and *Tom-Tom*. At the end of the project, a flight test campaign was carried out but it was very difficult for the pilots to control the aircraft especially regarding the connection in turbulence. In one flight, a fighter was actually torn away from the right wingtip of the middle aircraft. The project ended after this incident [8]. In addition to the publications of Vogt, other reports dealing with aerodynamic and aeroelastic phenomena in the project Tom-Tom exist [10–14].

In 1966, Raymond Prunty Holland, Jr. introduced the concept of an *Air Train* in the patent

filed under US3,249,322 [15]. Holland described a manned, wingtip-coupled formation with joints allowing yaw and roll motion. In addition, the joints are able to transfer fuel from one aircraft to another. Like Vogt, he proposes his configuration based on the reduction of stresses and weight with the goal of increasing the aerodynamic efficiency. Another patent relating to an aircraft docking has been filed by Gomez, Parks and Woodworth [16]. It describes a docking mechanism for two or more unmanned aerial vehicles that allows a roll motion between the aircraft.

In relation to the previously introduced projects, Samantha A. Magill investigated the dynamic behavior of coupled aircraft [17]. The focus is put on the stability of manned wingtip-docked flights. In 2009, Morrisey and McDonald discussed a method for the multidisciplinary design of an extreme-aspect-ratio unmanned HALE aircraft. They refer to an aircraft configuration of multiple wings as a *pinned-wing*. The dynamic behavior of the coupled system is undetermined. The design results are compared with the flight performance of the Helios. The investigation reveals that the weight can be decreased by 14.2 % for six coupled segments in comparison to the Helios [18]. In another study, Carlos Montalvo investigated the wingtip coupling of unmanned aircraft using passive magnets [19]. The focus of the analysis lies on the flight dynamic modeling of the coupled formation and the influence of the number of coupled aircraft on classical flight dynamics modes. He finds that when aircraft connect, the fundamental modes change and can become overdamped or even unstable. Furthermore, Montalvo developed control laws relating to coupled flights. However, he only takes a formation with rigid joints into account. As a consequence, the wingspan of the formation is increased but the structural dynamic effect of coupling is canceled out since the assumed model only considers the 6 rigid-body degrees of freedom [19]. In the patent filed under US6,641,082 in 2003, Bevilaqua and Tait describe a flight control system for coupled aircraft aimed at coupling two fighter aircraft to a ferrying aircraft [20]. The system follows the assumption that the ferrying aircraft controls the formation. Besides formation control, the flight control system also provides a disconnecting mode, if the aircraft formation becomes uncontrollable. A centralized control approach is used. The structure of the flight control laws is not described in detail.

In 2016, Geoffrey S. Sommer published the concept of an unmanned multibody aircraft as HAPS in the patent US9,387,926 [21]. He describes an aircraft system of several autonomous modular flyers using a wingtip-to-wingtip connection. The individual aircraft are initially carried to a certain altitude by balloons or a larger support aircraft. Then, they form a so-called skybase following rendezvous maneuvers. As a result, a high-aspect-ratio wing is established that reduces the induced drag. The wingtip hinges permit flapping of the individual aircraft and a potential loading does not cause separation. Sommer explains the complete life cycle of such a skybase with seven phases. Especially the loiter phase is worthwhile considering with respect to an application as HAPS. Due to the modularity of the skybase, aircraft with a malfunction can be separated from the formation and the rest of the skybase can continue the mission. In addition, the connection element of Sommer's patent also provides rules for separation due to a) gusts above a certain gust threshold, b) a turn of the multiple-articulated flying system or c) a span shear above a certain span shear threshold. In general, the connection element (bearing) allows two degrees of freedom of the aircraft relative to pitch and roll. In summary, despite the procedural descriptions in the patent, the vast majority of technological questions remain unsolved. A notable exception is that for trimming the aircraft about the longitudinal axis, a simple flight mechanical relation is introduced. Neither the effects of coupling on flight performance nor on flight dynamics are described [21].

Carithers and Montalvo give experimental results of flying unmanned connected aircraft. They investigated the design and flight test of two fixed wing aircraft connected at the wingtips. The flight control systems uses a PID-control law to keep the aircraft level in both pitch and roll [22]. Coupling of unmanned single aircraft is investigated in the NASA *Project Link!*. Cooper and Rothhaar describe a dynamic model and a control loop to connect two aircraft in the air [23]. Behrens et al. conducted experiments in the wind tunnel to determine the effect of wing-tip coupling to the lift distribution and aerodynamic moments. In addition, the authors validated the results with CFD calculations [24].

1.2 Objectives and Contributions of this Paper

Since 2014, TU Berlin's department of flight mechanics, flight control and aeroelasticity has been conducting research on the topic of multibody aircraft operating in high altitudes with long endurance. To delineate the term *multibody aircraft* from other concepts like the *pinned-wing* [18] or *meta aircraft* [22], it is defined as follows:

> *A multibody aircraft is an unmanned aircraft system (UAS) connecting several individual UAS at mission altitude with a mechanical joint to form a coupled aircraft structure with a high-aspect-ratio wing. It is suitable for operation at high altitudes. Each of the individual UAS has a small aspect ratio and either can climb on its own to mission altitude or it can be transported with a support technology like a balloon or a carrier aircraft.*

The fundamental differences between the multibody aircraft and a conventional rigid or flexible aircraft are the following:

1. A high-aspect-ratio wing is achieved through wingtip coupling of several individual aircraft with mechanical joints leading to an aircraft structure with multiple, distributed flight controls along the wingspan;
2. The number of the degrees of freedom is finite (depending on the joint configuration and the number of coupled aircraft);
3. The coupling equations between the aircraft are non-linear, but can be expressed mathematically exactly; and
4. The *formation modes* that occur due to the mechanical wingtip connection do not have any mechanical stiffness or damping and, hence, their eigenvalue and eigenvector characteristics depend only on the aerodynamics.

This paper summarizes the main research contribution in terms of flight mechanical modeling and design as well as flight control laws for a multibody aircraft. Details of special findings can be found in other publication referenced in this paper.

2 FLIGHT DYNAMIC MODEL

In aeroelasticity, the Collar diagram describes dynamic response problems of flexible aircraft through the interaction of inertial, elastic and aerodynamic forces [25]. Those forces also exist for multibody aircraft. The following section describes the assembling of the equation of motion with those three forces. The following assumptions are made:

1. The multibody aircraft consists of multiple single aircraft, all being individually rigid aircraft. Aeroelasticity of the single aircraft is not considered due to the structural design.

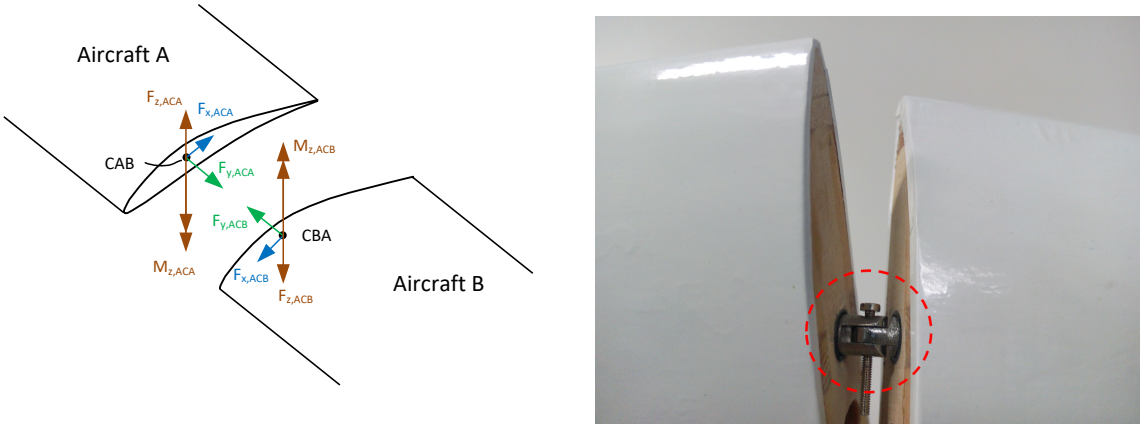

(a) Reaction forces and moments

(b) Physical implementation

Figure 3: Joint with pitch and roll degree of freedom between two aircraft

2. The aerodynamic forces are modeled using potential flow theory (vortex lattice method).
3. The engine is ideal. Energy dissipation due to friction is considered but impacts of propeller rotational speed and blade pitch angles are not considered.
4. Thrust force acts in x-direction of the body-fixed axes system without moment about the center of gravity of the single aircraft.
5. There is no gap between the aircraft. It is assumed that there is a seal, which prevents flow from the lower to the upper surface.
6. The joint connections between two single aircraft are considered to be ideal, i.e. without natural friction, damping or spring forces.

The equations of motion are derived using Kane's method [26]. They are formulated as:

$$\tilde{\mathbf{F}}_\mathrm{r} + \tilde{\mathbf{F}}_\mathrm{r}^\star = 0 \quad (r = 1, \ldots, p) \;, \tag{1}$$

where $\tilde{\mathbf{F}}_\mathrm{r}$ is the vector of the generalized active forces, $\tilde{\mathbf{F}}_\mathrm{r}^\star$ is the vector of the generalized inertial forces in the reference frame and p is the number of the generalized speeds. In Eq. 1, the denotation "generalized force" includes inertial and active forces as well as inertial and active moments (translation and rotation) [26]. Referring to the Collar triangle, those active forces and moments are caused by the aerodynamics and the elastic forces at the joints.

2.1 Inertial Forces and Generalized Speeds

The generalized inertial force is determined with

$$\tilde{\mathbf{F}}_\mathrm{r}^\star = -\sum_{j=1}^{l} {}^N\mathbf{F}_\mathrm{k}^{CG,j} \, \frac{\partial {}^N\mathbf{v}^{CG,j}}{\partial u_\mathrm{r}} - \sum_{j=1}^{l} {}^N\mathbf{M}_\mathrm{k}^{CG,j} \, \frac{\partial {}^N\omega^{B,j}}{\partial u_\mathrm{r}} \;, \tag{2}$$

where ${}^N\mathbf{v}^{CG,j}$ is the velocity of the center of gravity (CG) of the jth body in the Newtonian frame, ${}^N\omega^{B,j}$ the angular velocity of the body frame about the Newtonian frame of the jth body, u_r are the generalized speeds, and $\mathbf{F}_\mathrm{k}$ and $\mathbf{M}_\mathrm{k}$ are force and moment of the jth body decomposed as

$${}^N\mathbf{F}_\mathrm{k}^{CG} = m \left(\frac{d \, {}^B\mathbf{v}^{CG}}{dt} + {}^N\omega^B \times {}^B\mathbf{v}^{CG} \right) \quad \text{and} \quad {}^N\mathbf{M}_\mathrm{k}^{CG} = \mathbf{I} \, {}^N\dot{\omega}^B + {}^N\omega^B \times \left(\mathbf{I} \, {}^N\omega^B \right) \;, \tag{3}$$

with l representing the number of rigid bodies in the system. The generalized speeds depend on the motion constrains due to the joint. Fig. 3(a) shows the free-body diagram for the selected joint configuration that allows a pitch and roll motion between the aircraft. At the joints, the nonholonomic motion constraints

$$\begin{aligned} \left({}^{N}\mathbf{v}^{CAB} - {}^{N}\,\mathbf{v}^{CBA}\right)\vec{e}_{\mathrm{x,g}} = 0\,, \qquad \left({}^{N}\mathbf{v}^{CAB} - {}^{N}\,\mathbf{v}^{CBA}\right)\vec{e}_{\mathrm{y,g}} = 0\,, \\ \left({}^{N}\mathbf{v}^{CBA} - {}^{N}\,\mathbf{v}^{CAB}\right)\vec{e}_{\mathrm{z,g}} = 0\,, \qquad \left({}^{N}\omega^{A} - {}^{N}\,\omega^{B}\right)\vec{e}_{\mathrm{z,g}} = 0\,, \end{aligned} \tag{4}$$

are valid with ${}^{N}\mathbf{v}^{CAB}$ as body-fixed velocity of the point CAB (${}^{N}\mathbf{v}^{CBA}$ of point CBA) in the Newtonian reference frame, $\vec{e}$ as unit vector of the Newtonian reference frame and ${}^{N}\omega^{A}$ of aircraft A (${}^{N}\omega^{B}$ of aircraft B) as angular velocity in the Newtonian reference frame. For this configuration, the non-linear differential equations of motions that describe the dynamic behavior of the multibody aircraft can be expressed by a first-order non-linear differential equation system that consists of

- **12** non-linear first-order differential equations for the rigid-body motion (velocity, position, rotation rates and Euler angles) and
- **5** non-linear first-order differential equations for every coupled aircraft (roll and pitch rate as well as Euler angles).

For the flight dynamic analysis, the navigation differential equations (position and yaw angle for the rigid-body motion as well as yaw angle for every coupled aircraft) can be neglected. This reduces the number of differential equations to eight for the rigid-body motion and to four for every coupled aircraft. In the case of the reference aircraft (ten coupled aircraft), 44 first-order differential equations remain.

2.2 External Forces and Moments

The generalized active force of Eq. 1 is given by

$$\tilde{\mathbf{F}}_{\mathrm{r}} = \sum_{j=1}^{l} {}^{N}\mathbf{F}_{\mathrm{a}}^{\mathrm{CG,j}}\,\frac{\partial^{N}\mathbf{v}^{CG,j}}{\partial u_{\mathrm{r}}} + \sum_{j=1}^{l} {}^{N}\mathbf{M}_{\mathrm{a}}^{\mathrm{CG,j}}\,\frac{\partial^{N}\omega^{B,j}}{\partial u_{\mathrm{r}}}\,, \tag{5}$$

where $\mathbf{F}_{\mathrm{a}}$ and $\mathbf{M}_{\mathrm{a}}$ are the active forces and moments acting at the center of gravity. As external forces, the aerodynamic forces in a body-fixed reference system $\mathbf{R}_{\mathrm{A,b}}$, thrust $\mathbf{T}_{\mathrm{b}}$ in a body-fixed system and weight in the geodetic reference systems $\mathbf{W}_{\mathrm{n}}$ have to considered for every aircraft. The active force at the jth aircraft in the body-fixed reference frame is then determined as

$${}^{\mathrm{b}}\mathbf{F}_{\mathrm{a}}^{\mathrm{CG,j}} = \mathbf{R}_{\mathrm{A,b,j}} + \mathbf{T}_{\mathrm{b,j}} + \mathbf{T}_{\mathrm{b,n,j}}\,\mathbf{W}_{\mathrm{n,j}}\,, \tag{6}$$

where $\mathbf{T}_{\mathrm{b,n}}$ is the transformation matrix from the Newtonian/geodetic reference frame (index n) to the body-fixed reference frame. Applying the introduced assumptions, the aerodynamic moment in the body-fixed system $\mathbf{M}_{\mathrm{A,b}}$ is the only generalized external moment. Hence, the active moment of the jth aircraft in the body-fixed reference frame is

$${}^{\mathrm{b}}\mathbf{M}_{\mathrm{a}}^{\mathrm{CG,j}} = \mathbf{M}_{\mathrm{A,b,j}}\,. \tag{7}$$

The aerodynamic forces and moments are calculated using the vortex lattice method for every aircraft [27].

As introduced, the main difference between a conventional and flexible aircraft is the spring stiffness. An adjustment of the springs allows transforming a multibody aircraft model to a rigid

aircraft. This is used in the later flight control law design process. To represent stiffness and damping at the joints, elastic moments are introduced at the joints. For every joint connecting an aircraft j with an aircraft $j+1$, the effect of the spring on the roll motion (bending) is modeled using the moment $M_{\mathrm{s},\Phi}$ and the effect on the pitch motion (torsion) using the moment $M_{\mathrm{s},\Theta}$ with

$$\begin{array}{rcl} M_{\mathrm{s},\Phi} & = & k_\Phi \left(\Phi_j - \Phi_{j+1}\right) \\ M_{\mathrm{s},\Theta} & = & k_\Theta \left(\Theta_j - \Theta_{j+1}\right) \end{array}, \tag{8}$$

where k_Φ and k_Θ are spring constants and Θ and Φ are the pitch and bank angle. The same procedure is carried out for the damping moments using the roll rate p and the pitch rate q. The damping moments for the rolling and pitching moment are

$$\begin{array}{rcl} M_{\mathrm{d},\Phi} & = & d_\Phi \left(p_i - p_{i+1}\right) \\ M_{\mathrm{d},\Theta} & = & d_\Theta \left(q_i - q_{i+1}\right) \end{array}. \tag{9}$$

These moments act in the Newtonian reference frame and are added to the active moments of Eq. 7 with

$${}^{\mathrm{b}}\mathbf{M}_{\mathrm{a}}^{\mathrm{CG,j}} = \mathbf{M}_{\mathrm{A,b,j}} + \mathbf{T}_{\mathrm{b,n,j}} \begin{bmatrix} M_{\mathrm{d},\Phi,j-1} + M_{\mathrm{s},\Phi,j-1} - M_{\mathrm{d},\Phi,j} - M_{\mathrm{s},\Phi,j} \\ M_{\mathrm{d},\Theta,j-1} + M_{\mathrm{s},\Theta,j-1} - M_{\mathrm{d},\Theta,j} - M_{\mathrm{s},\Theta,j} \\ 0 \end{bmatrix}, \tag{10}$$

where $\mathbf{T}_{\mathrm{b,n}}$ is the transformation matrix from the Newtonian/geodetic reference frame (index n) to the body-fixed reference frame. Eq. 10 represents a general formulation for the case that the considered aircraft is coupled with other aircraft on the left and right wingtip. If there is only a one-sided coupling, only one damping and spring moment for pitch and roll motion must be considered.

2.3 Non-Linear Equations of Motion

The non-linear equations of motion, which include the computation of the aerodynamics with the vortex lattice method, and the kinematic relations must be solved numerically. This leads to a system

$$\dot{\mathbf{x}} = \mathbf{f}\left(\mathbf{x}, \mathbf{u}, \mathbf{z}\right) \tag{11}$$

with $\mathbf{x}$ as state vector, $\mathbf{u}$ as input vector and $\mathbf{z}$ as disturbance vector. The non-linear function $\mathbf{f}\left(\mathbf{x}, \mathbf{u}, \mathbf{z}\right)$ represents the dynamic behavior. If the actual positioning within the formation is neglected, one aircraft (the master one) leads to eight states. If yaw angle of the coupled aircraft is also neglected, every coupled aircraft leads to four additional states (roll and pitch motion). The elevator deflection η, the left ξ_{left} and right ξ_{right} aileron deflections, the rudder ζ and the thrust F of every aircraft are used as input variables. The wind is considered as disturbance. It is assumed that a vertical and horizontal wind component can act at each aircraft. This leads to a total of 20 disturbance variables.

3 FLIGHT PERFORMANCE OF A MULTIBODY HAPS AIRCRAFT

The flight performance design of the multibody aircraft flying at high altitudes over a long period to operate as HAPS shall comply with the specifications of the DARPA Vulture program. The payload capacity shall be 450 kg. Its operation requires a 5 kW power supply for 24 h. The payload may be distributed across the aircraft or integrated in a single location. In general, the endurance depends on the solar energy at operation latitude for the winter solstice. If the system's required energy is smaller than or equal to the solar energy of the winter solstice and

the batteries are able to provide sufficient energy at night, a 24-hour operation on 365 days a year is possible. The service time of the system for more than one year depends on the individual operational life of individual elements such as solar cells and energy storage system. From a flight mechanical point of view, an endurance of one year has thus to be proven in the design process. The design latitude is specified at $40°$ N/S in the Vulture program. Coupling and decoupling shall be carried out at mission altitude. As a consequence, each single aircraft of the formation has to fulfill the flight performance requirements for stand-alone operation. The single aircraft shall have a rigid structure to neglect aeroelastic effects [28, 29].

3.1 Design Process

A successful design for the introduced requirement is established, if the energy balance is fulfilled and steady conditions of Eq. 11 are achieved. Especially for the energy balance there are strong dependencies of the parameters among each other. An analytical solution is not possible and, hence, a numerical iteration method is used to find a suitable design.

3.1.1 Energy Balance

The energy equation has to be considered regarding the flight performance of solar-powered HAPS aircraft. The available solar energy has to be greater than or equal to the required energy of the aircraft E_{req} that comprises the propulsion energy and the energy consumption of the payload. This is expressed mathematically using

$$E_{\text{sun}} = E_{\text{req}} \tag{12}$$

with E_{sun} as available solar energy. Below, only the propulsion energy is considered. Both solar energy and propulsion energy are expressed by the integral of the power over the time. The solar energy results from the integration of the product between solar power density $\overline{P}_{\text{sun}}$, solar area S, which is assumed to be equal to the wing area, and solar cells efficiency η_{solar} over the time between sunrise and sunset. The required propulsion energy results from the integration of the required power that corresponds to the product of drag D, flight path velocity V_K and propulsion efficiency η_{V}. The insertion of those relationships in Eq. 12 leads to

$$\eta_{\text{solar}} S \int_{t_{\text{sun rise}}}^{t_{\text{sun set}}} \overline{P}_{\text{sun}}\, dt = \frac{1}{\eta_{\text{V}}} \int_{0\text{ h}}^{24\text{ h}} D\, V_K\, dt\,. \tag{13}$$

The drag comprises zero lift drag D_0 and induced drag D_{i}. The induced drag is calculated by Prandtl's lifting-line theory stating an increase of the induced drag with the square of the lift coefficient. Thus, the total drag coefficient C_{D} is calculated by

$$C_D = \underbrace{C_{D0}}_{\text{zero-lift drag}} + \underbrace{k\, C_L^2}_{\text{induced drag}} \quad \text{with} \quad k = \frac{1}{\pi\, \Lambda\, e}\,, \tag{14}$$

with C_{D0} as zero lift drag coefficient, C_L as lift coefficient, Λ as aspect ratio and e as Oswald factor. The lift coefficient for straight and level flight results from the lift/weight equilibrium. Assuming no wind $V_K = V_A = V$ and a constant airspeed V over the whole day results in

$$\eta_{\text{solar}} S \int_{t_{\text{sun rise}}}^{t_{\text{sun set}}} \overline{P}_{\text{sun}}\, dt = \frac{1}{\eta_{\text{V}}} \frac{\rho}{2} V^3 S \left(C_{D0} + k \underbrace{\frac{4\, m^2\, g^2}{V^4\, \rho^2\, S^2}}_{C_L^2} \right) t_{\text{day}}\,, \tag{15}$$

with ρ as air density, m as total mass, g as gravity constant, and t_{day} as duration of one day in seconds ($86,400$ s). Using the modified wing loading $\frac{W}{S} = \frac{m\,g}{S}$ and integration of the solar power density to the solar energy density $\overline{E}_{\text{sun}}$, transforms Eq. 15 to

$$\overline{E}_{\text{sun}} = \frac{1}{\eta_{\text{V}}\ \eta_{\text{solar}}} \left(\frac{\rho}{2} V^3 C_{D0} + \frac{2\,k}{V\ \rho} \frac{W^2}{S} \right) t_{\text{day}}\ . \tag{16}$$

This is the fundamental flight performance equation for solar-powered aircraft with continuous operation. The solar energy density depends on the operation latitude and the length of the day. In case of a year-long operation, the winter solstice has to be considered as worst-case scenario. With the exception of air density and efficiency factors, all other parameters depend on the aircraft design. The wing loading depends on the aspect ratio (structural weight), dynamic pressure (structural weight) and the required power (engine). The zero lift coefficient depends on the sizing of aircraft. Those dependencies lead to a strong interaction between the parameter and require a numerical iteration method to get a successful design. Models for the structural weight and the zero lift coefficient are taken from Raymer [30], Roskam [31] and Torenbeek [32].

The multibody aircraft shall operate as unmanned. Most of aircraft design literature contains structural design models only for fighter, cargo aircraft and general-aviation aircraft. Detailed statistical weight models for UAS do not exist in the literature. Sóbester et al. [33] provides a statistical model with

$$\frac{W_{\text{empty, UAS}}}{W_{\text{TOW}}} = 0.916\ W_{\text{TOW}}^{-0.0795} \tag{17}$$

as relation between empty weight $W_{\text{empty, UAS}}$ and maximum take-off weight W_{TOW} that is the result of a regression fit of 30 UAS. Raymer also provides a general relation between empty weight $W_{\text{empty, GA}}$ and maximum take-off weight W_{TOW} for general aviation aircraft with

$$\frac{W_{\text{empty, GA}}}{W_{\text{TOW}}} = (0.8578\text{–}0.0333\ \log\left(W_{\text{TOW}}\right))\ W_{\text{TOW}}. \tag{18}$$

For different maximum take-off weights, the empty weight as fraction of the total weight strongly differs between UAS and general-aviation aircraft. Since detailed mass models are only available for general-aviation aircraft, those models have to be corrected by the factor

$$f_{\text{weight correction}} = \frac{W_{\text{empty, UAS}}}{W_{\text{empty, GA}}} \tag{19}$$

that is the ratio between the empty weights of the UAS and of a general-aviation aircraft for the same maximum take-off weight.

In case of conventional aircraft, the right-hand side of Eq. 16 will be small if the aircraft operates at the airspeed of minimum required power. This airspeed is not flyable, because a boundary exists for a maximum aspect ratio when flying with minimum required thrust or power. The limit can be expressed by the inequalities

$$\begin{aligned} C_{L,\text{min, D}} &< C_{L,\text{max}}\ , \\ C_{L,\text{min, P}} &< C_{L,\text{max}}\ . \end{aligned} \tag{20}$$

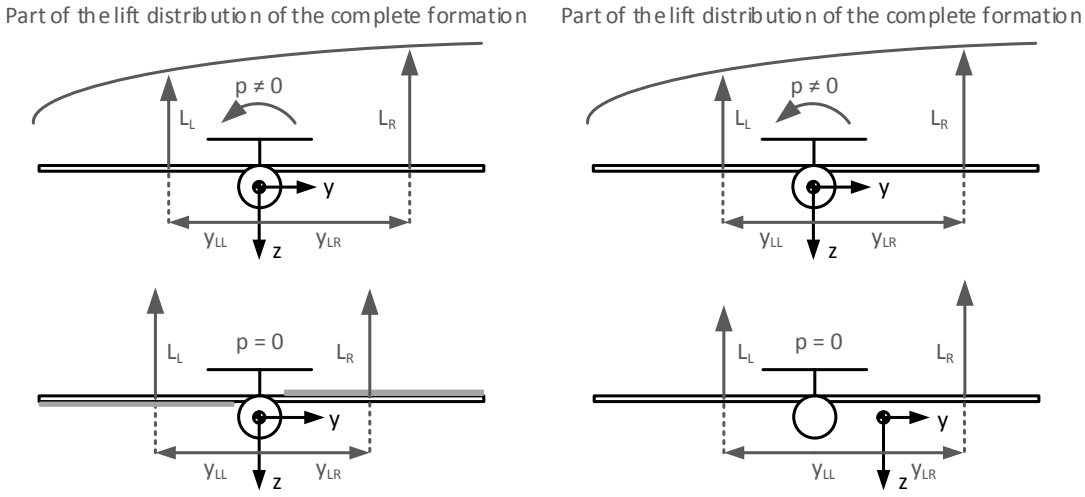

Figure 4: Trim methods to compensate an undesired roll motion on the single aircraft

With the lift coefficient for minimum required thrust

$$C_{L,\text{Dmin}} = \sqrt{\frac{C_{D,0}}{k}}\,. \tag{21}$$

and the lift coefficient for minimum required power

$$C_{L,\text{min P}} = \sqrt{\frac{3\,C_{D,0}}{k}}\ , \tag{22}$$

those inequalities lead to a bound for the aspect ratio of

$$\Lambda < \frac{C_{L,\text{max}}^2}{\pi\, C_{D,0}\, e} \tag{23}$$

for minimum drag (minimum required thrust) and

$$\Lambda < \frac{1}{3}\frac{C_{L,\text{max}}^2}{\pi\, C_{D,0}\, e} \tag{24}$$

for minimum required power.

3.1.2 Trimming the formation

In addition to fulfillment of the energy balance, the left side of Eq. 11 has to become zero for a successful design. This means that the external forces and moments are in balance. The angle of attack for the complete formation, elevator deflection and the battery's lateral center of gravity for each aircraft are modified to ensure that external forces (lift and weight) and aerodynamic moments are in equilibrium. The establishment of the flight with the desired lift coefficient is carried out by changing the angle of attack. The elevator deflections ensure zero pitching moments for each individual aircraft. The shift of the lateral position of the battery mass is used for abolishing the rolling moments. This approach differs from traditional aircraft where rolling moments are suppressed by aileron deflections. Fig. 4 shows both methods by considering one

Table 1: Selected parameters for the optimized multibody aircraft with planar wing

Span [m]	210.66				
Aspect ratio [1]	55				
Total mass [kg]	4509				
Total battery mass [kg]	1137				
Altitude [m]	20,000				
Airspeed [m s^{-1}]	33.37				
Horizontal tail area [m^2]	6.05				
Vertical tail area [m^2]	1.45				
zero-lift drag coefficient [1]	0.008				
Available sun energy per design day [GJ/day]	11.12				
Required sun energy per design day [GJ/day]	11.12				
Max. engine power [kW]	11.51				
Long. CG position [m]	-3.74				
Neutral point wing [m]	-3.26				
Distance wing tail [m]	11.49				
Half span per aircraft [m]	10.53				
Moment of inertia per aircraft [kg m^2]	$\begin{pmatrix} 7977 & 0 & -231 \\ 0 & 6937 & 0 \\ -231 & 0 & 14691 \end{pmatrix}$				
	AC1	AC2	AC3	AC4	AC5
Angle of attack [1°]	4.8	4.8	4.8	4.8	4.8
Elevator deflection [1°]	-3.58	-6.05	-6.4	-6.51	-6.55
Trim engine power [kW]	5.29	2.04	1.49	1.29	1.22
Lat. CG position [m]	1.69	2.12	1.68	1.05	0.36
Battery shift [m]	6.7	8.39	6.65	4.17	1.42

Note: The design day is the day with lowest available sun energy.

aircraft of the formation. The elliptic lift distribution of the complete formation leads to a difference in the resulting lift at the left L_L and right L_R wing of each aircraft. Additionally, the force acting points of the left-hand side x_LL and the right-hand side x_LR are different. As a consequence, a roll acceleration $\dot{p}$ occurs. To avoid this motion, the relation

$$\frac{y_\mathrm{LR}}{L_\mathrm{L}} = \frac{y_\mathrm{LL}}{L_\mathrm{R}} \tag{25}$$

has to be satisfied. This balance can be achieved by means of flap deflection, see Fig. 4 (left). On the right wing, a positive flap deflection results in a lift increase. On the left wing, a negative flap deflection decreases the lift. Both acting points are shifted slightly. On the one hand, this method satisfies Eq. 25, but on the other hand, the lift distribution is influenced and the additional flap deflections lead to drag. The method shown in Fig. 4 (right) shifts the center of gravity to the left wing. The resulting lift forces on the right and left wing are not impacted, but their lever arms are. This fulfills Eq. 25 without changing the lift distribution.

3.2 Design Result

The optimization result for a multibody aircraft with planar wing is a formation of ten coupled aircraft with a wingspan of 211 m and a total mass of 4,509 kg. Selected parameters are listed in Tab. 1 with *AC1* referring to the aircraft at the outer side and *AC5* referring to the aircraft at

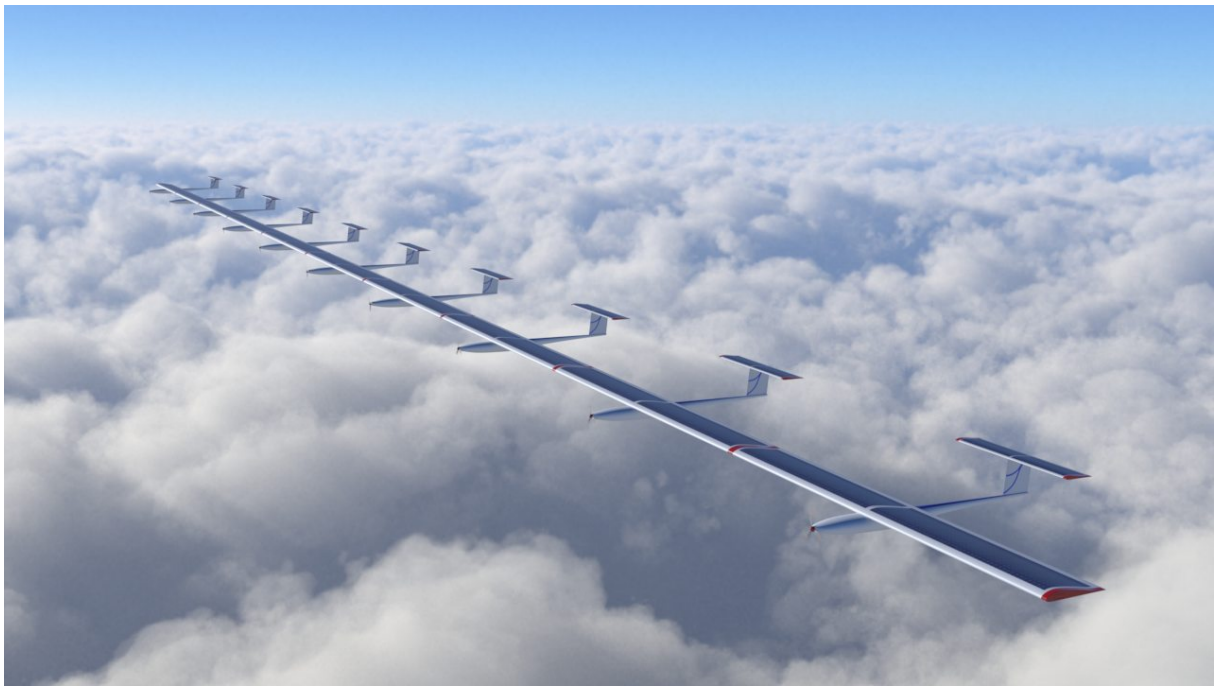

Figure 5: Illustration of the optimized multibody HAPS aircraft with planar wing

the inner side of the left part of the formation. Fig. 5 shows the multibody aircraft in flight. The thrust is not uniformly distributed for the multibody aircraft configuration. The outer aircraft require a higher engine power than the inner ones. This is due to the fact that the local drag at the outer aircraft is higher than the local drag at the inner aircraft. The lift distribution of a rectangular wing with low aspect ratio is nearly elliptic. With increasing aspect ratios, the elliptic distribution converges to a rectangular one. Lower lift in direction to the wingtips is caused by higher induced angle of attack. Higher induced angle of attack leads to higher induced drag. The thrust is used to locally compensate the drag. For trimmed condition, the sum of all engines has to compensate the total drag. This means that a uniformly distributed thrust can be used as well. The joints transmit all forces. As drag and thrust do not compensate each other anymore, higher shear forces occur at the joints.

A further notable aspect is the center of gravity shift. The maximum required shift of the battery lies within the limits of the half-span. Because of the lift distribution, the inner aircraft of the formation have to carry parts of the weight of the outer aircraft. Because *AC1* has less lift than weight, the vertical reaction force compensates that difference and leads to a vertical force balance. The reaction force acts at the joint and a rolling moment occurs at the lever arm with respect to the center of gravity of *AC1*. The total rolling moment that has to be compensated by lateral center of gravity shift is the sum of the rolling moment caused by the reaction forces and the rolling moment caused by different left-side and right-side wing lift. In case of *AC2*, this shift is even larger. Because the joint between *AC1* and *AC2* leads to a negative force at *AC1*, a force of the same magnitude but with a positive sign occurs at *AC2*. With respect to the force balance in vertical direction, the lift has to compensate the weight of *AC2* and the reaction force between *AC1* and *AC2*. Because the magnitude of lift is too small at *AC2*, the third aircraft establishes the vertical force balance of *AC2* with a reaction force pointing in negative direction. The left-side and right-side reaction forces of *AC2*, hence, point in different directions. Because the forces act at the left and right side of the center of gravity, respectively, the resulting rolling moment has the same sign. In combination with the left-side and right-side wing lift imbalance,

the induced rolling moment is now higher in magnitude. Hence, the difference between center of gravity and center of rotation increases. Because *AC3*, *AC4* and *AC5* generate more lift than weight and the left-side and right-side lift balance is smaller, the induced rolling moment is also smaller.

3.3 Improvement of Flight Performance

The multibody aircraft configuration allows different pitch and bank angle of the individual aircraft. In the reference configuration of the planar wing, all individual aircraft have the same pitch and bank angle. An alternative is the drag-reduced configuration with a nearly elliptical lift distribution to further decrease the induced drag.

Besides the aspect ratio, the Oswald factor influences the induced drag. The Oswald factor is a correction factor that represents the change in drag with lift of a wing, as compared with an ideal wing having the same aspect ratio and an elliptical lift distribution [30]. Empirical models of Raymar [30] and Obert [34] show a reduction of the Oswald factor with increasing aspect ratio for rectangular wings. Following Prandtl's classical lifting-line theory, an elliptic wing without twist produces minimum induced drag. For any other planform, an untwisted wing is optimal only at zero lift [35]. The change in the wing shape due to twist affects the lift distribution and leads to a higher Oswald factor. In case of a continuous wing, geometrical twist and dihedral are easy to implement. In case of coupled aircraft, only a discrete twist and dihedral can be achieved by changing the pitch and bank angle of the aircraft. To accomplish the highest possible Oswald factor for the multibody aircraft configuration, a numerical study with the vortex lattice computation is conducted to identify an optimal wing shape with twist. The findings are as follows:

- Different pitch angles (twist) have a significant influence on the Oswald factor;
- The optimal pitch angle of the individual aircraft decreases starting from the center of the formation towards the wingtip;
- The higher the aspect ratio, the higher is the induced drag reduction by twist;
- The higher the number of coupled aircraft, the higher is the increase of the Oswald factor; and
- A general twist rule can be derived from the results irrespective of the aspect ratio and the number of coupled aircraft.

This general twist rule is only a function of the normalized span

$$\eta = \frac{2\,y}{b_{\text{max}}}. \tag{26}$$

and results from curve fitting for configurations with 10, 12 and 14 coupled aircraft and aspect ratios between 30 and 60, respectively, in each case with

$$\Theta_{\text{twist}}\left(\eta\right) = -0.1614\eta^2 + 0.0490\eta - 0.0046\,. \tag{27}$$

The twist rule is now applied to the reference multibody aircraft configuration of Tab. 1. All other geometrical and inertial parameters (with exception of the lateral center of gravity position) as well as the airspeed remain constant and the configuration is trimmed. Although the required energy is only 91.5 % of the reference case, the required lateral center of gravity shift is very high and exceeds the limitation of the half-span. Taking the maximum shift of 10.527 m into account, a scaled twist of Eq. 27 can be applied. With this, the required energy is reduced by 0.96 %.

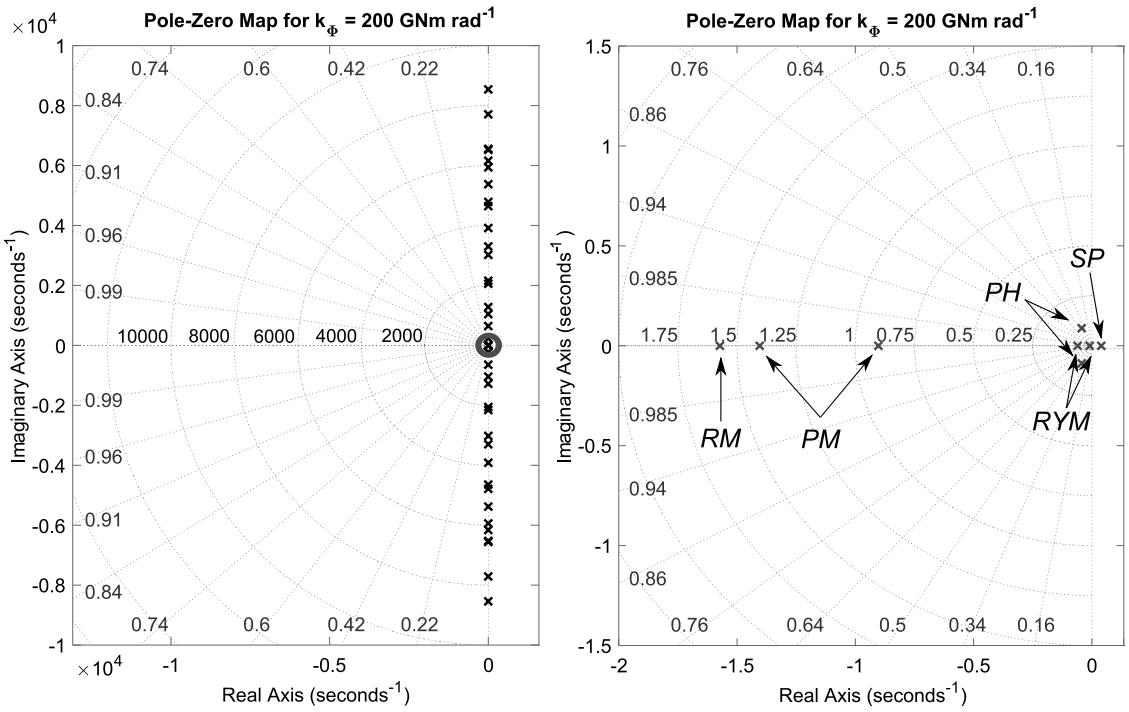

(a) Overall view

(b) Detail view with rigid-body modes

Figure 6: Eigenvalues in the complex plane for spring stiffness of $k_\Phi = 200$ GNm rad^{-1} and $k_\Theta \approx 76.9$ GNm rad^{-1}.

4 FLIGHT DYNAMICS OF A MULTIBODY HAPS AIRCRAFT

The linearized flight dynamic equations of the formation are used for the evaluation. Based on the eigenvalues and eigenvectors, the eigenmodes of the formation are classified and an assessment of the flight dynamics is conducted. First, this evaluation is carried out for the flight dynamics with the modeled hypothetical spring elements between the aircraft. A very high stiffness corresponds to a classical rigid-body aircraft. Afterwards, the stiffness is reduced in discrete steps until a value of zero, which corresponds to the applied joint technology.

4.1 Model with Elastic Moments at the Joints

In case of a high very high roll stiffness $k_\Phi = 200$ GNm rad^{-1} and torsional stiffness $k_\Theta = 76.9$ GNm rad^{-1}, the resulting eigenvalues of the linearized state-space system are similar to that one of a conventional aircraft. The eight flight mechanical eigenvalues have a low frequency or a low time constant while the structural eigenvalues are distributed along the $j\omega$-axis far away from the origin of the complex plane. Fig. 6 shows the eigenvalue distribution in the complex plane. The computed flight dynamics modes have only one complex conjugate pair of eigenvalues. All other eigenvalues are aperiodic. The assignment of the modes is conducted with the help of the eigenvectors. In longitudinal motion, the phugoid is identified as oscillation with the complex conjugate eigenvalue. The dominating states are pitch angle and velocity. The short period mode is not an oscillation. Two aperiodic poles describe the pitch motion of the aircraft. The aperiodic behavior is caused by an aftwards location of the center of gravity. The Dutch roll is also characterized by two real poles. Here, they are named yaw-roll motion. The high damping is due to the large directional stability. The dominating states in the eigenvectors are sideslip angle and bank angle. In addition, the yaw rate and (with a smaller magnitude) the roll rate are involved. The assignment is made using the different sign of bank and sideslip angle as well as the different sign for roll and yaw rate. The spiral mode is characterized by a strong

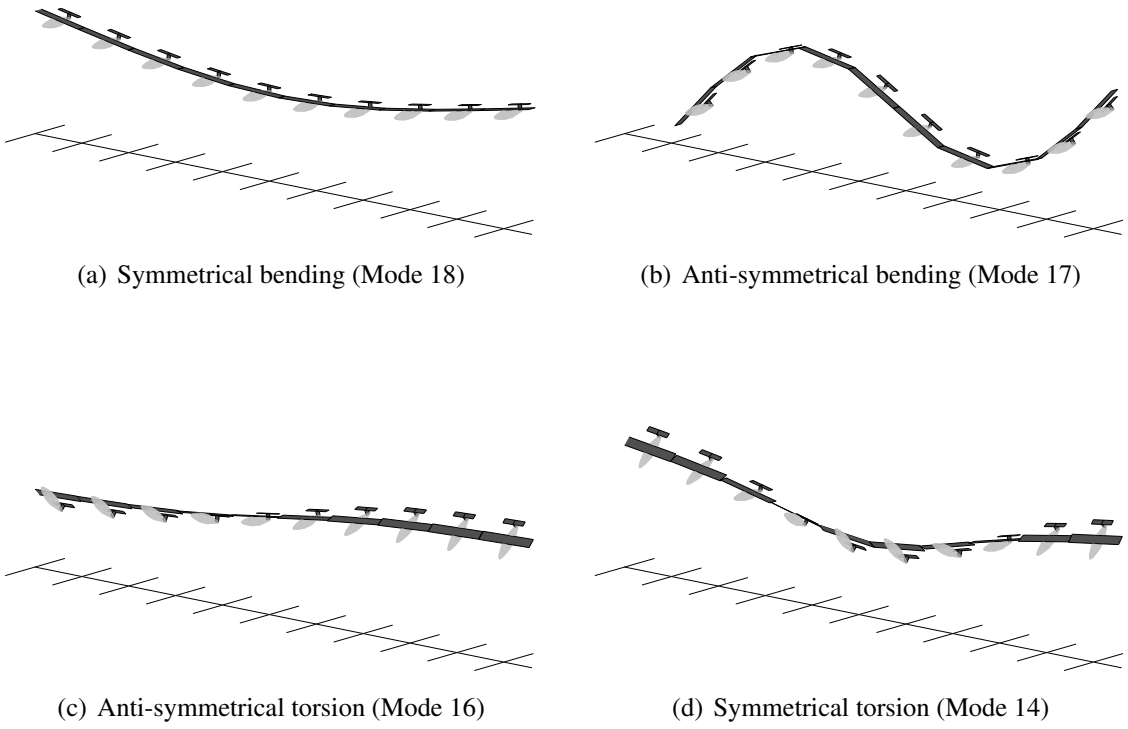

(a) Symmetrical bending (Mode 18)

(b) Anti-symmetrical bending (Mode 17)

(c) Anti-symmetrical torsion (Mode 16)

(d) Symmetrical torsion (Mode 14)

Figure 7: Selected eigenvectors of the formation modes for every kind of motion and a for spring stiffness of $k_\Phi = 200$ GNm rad^{-1} and $k_\Theta \approx 76.9$ GNm rad^{-1}

impact of sideslip and bank angle. In contrast to the yaw-roll motion, sideslip and bank angle point in the same direction. In all rigid-body modes, an impact of structural motion (bending or torsion) cannot be observed.

In Fig. 7, the formation modes for a symmetrical bending (roll motion), anti-symmetrical bending (roll motion), symmetrical torsion (pitch motion) and anti-symmetrical torsion (pitch motion) are shown for the nominal center of gravity position. The maximum value for the largest eigenvector element is set to $45°$[1]. The eigenmodes look similar to the ones of a conventional beam.

4.2 Desired Configuration (No Elastic Moments at the Joints)

Fig. 8 shows the eigenvalues of a linearized system with no spring (second case) and, in addition, the identified rigid-body modes of the reference case ($k_\Phi = 200$ GNm rad^{-1}). The rigid-body modes are identified with the help of the eigenvectors. The pitch mode, phugoid and spiral eigenvalues can be detected, while an identification of the roll mode and the Dutch roll is not unequivocally possible. Eigenvalues of formation modes and rigid-body modes are close together. In contrast to the reference case, the system with no spring elements has eight complex conjugate eigenvalues (four modes) on the right-hand side. The interference between rigid-body modes and formation modes also becomes clear in simulation studies. Using the same inputs that lead to a roll maneuver, the bank angle response is illustrated in Fig. 9 for the surrogate multibody dynamics with hypothetical springs and the multibody dynamics with-

[1]For mode 18, a maximum value of $10°$ is used for the representation

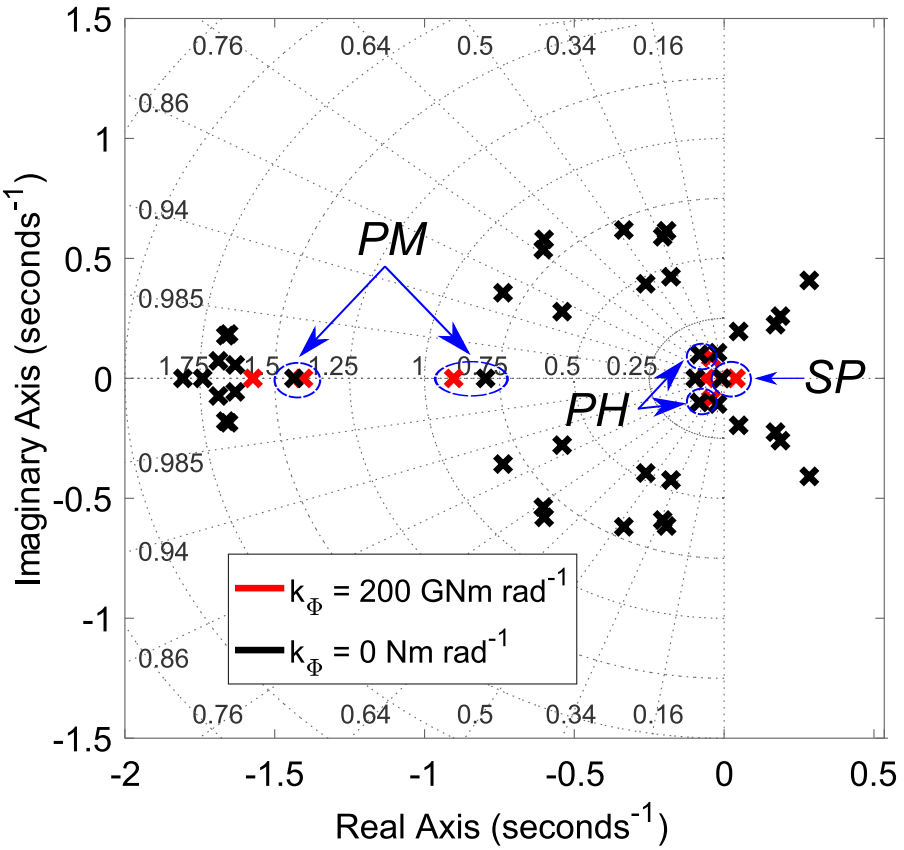

Figure 8: Eigenvalues for the joint without spring elements and rigid-body eigenvalues of the reference case with a spring stiffness of $k_\Phi = 200$ GNm rad^{-1}

out spring. While in the case with spring elements all bank angles have the same magnitude, differences occur in the case without spring and a roll maneuver seems to be impossible.

5 FLIGHT CONTROL FOR A MULTIBODY HAPS AIRCRAFT

The top-level requirements for the flight control laws of the multibody aircraft are i) reaching and holding an altitude, ii) reaching and holding a heading, iii) holding speed to avoid stall and iv) gust rejection. Fig. 10 shows a control law structure that is suitable to achieve those requirements.

A formation of ten aircraft with joints that do not transmit rolling and pitching moments has 24 degrees of freedom (3 translational degrees of freedom and 21 rotational degrees of freedom) and 50 inputs. That means that there are more inputs available than actually required to influence all degrees of freedom. Such so-called over-actuated systems are handled using control allocation. The main idea of aircraft control allocation is as follows. The control design is not carried out by directly using the aerodynamic surfaces or thrust. Rather, inputs of the aircraft are expressed (indirectly) by moments and forces or their equivalent accelerations and rotational accelerations acting on the aircraft. Those inputs are referred to as *virtual* inputs. In case of the multibody aircraft, the following 24 virtual inputs are used:

- **3** derivatives of the generalized speeds for the translational motion of the fifth aircraft (as reference aircraft),
- **1** derivative of the generalized speed for the yaw motion of the reference aircraft,
- **10** derivatives of the generalized speeds for the roll motion of every aircraft, and

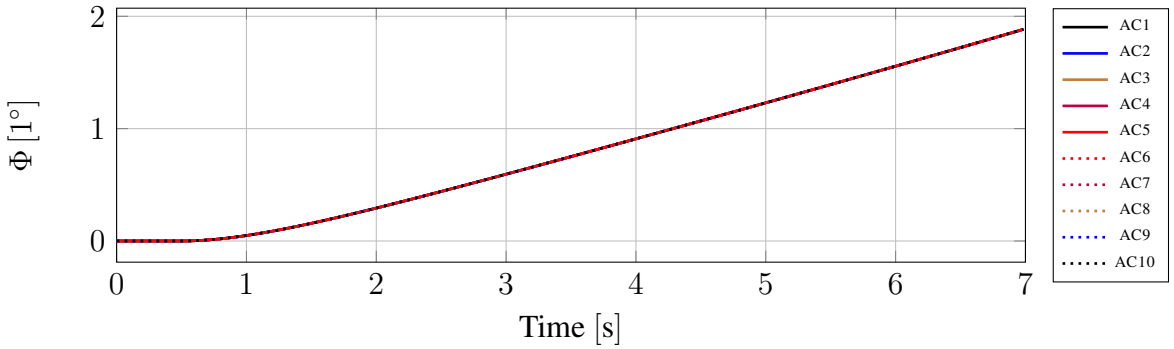

(a) Artificial multibody aircraft dynamics

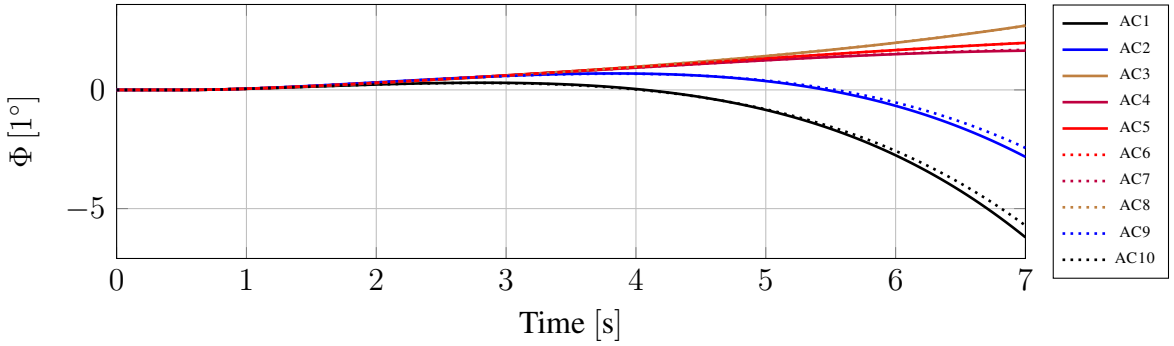

(b) Multibody aircraft dynamics

Figure 9: Non-linear step response for a roll maneuver

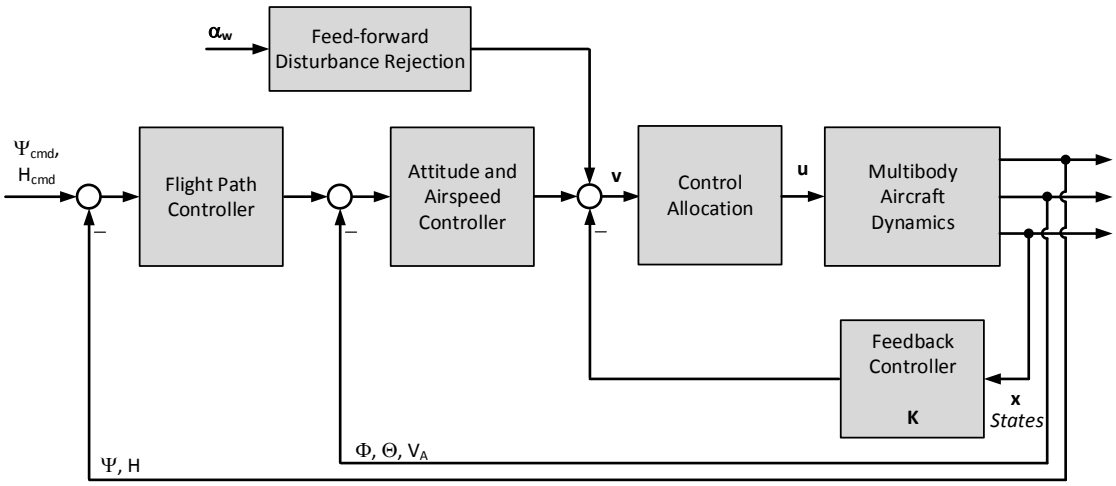

Figure 10: Flight control law structure for the multibody aircraft

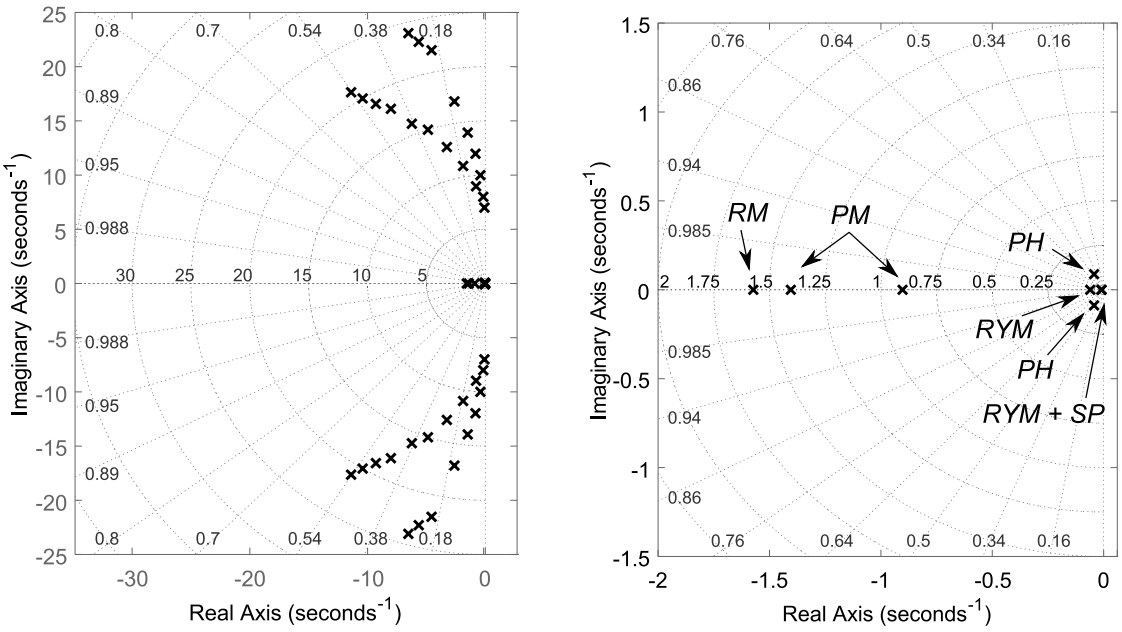

(a) All eigenvalues

(b) Flight mechanics modes

Figure 11: Eigenvalues of the multibody aircraft's flight dynamics after applying eigenstructure assignment (Kind of rigid-body motion: RM - roll mode, PM - pitch motion(two aperiodic short period modes), RYM - roll-yaw motion, SP - spiral mode, PH - phugoid)

- **10** derivatives of the generalized speeds for the pitch motion of every aircraft.

With this, an input for every degree of freedom is available.

With a mapping matrix, the non-square state space model of the multibody aircraft is transferred to a squared system description. With this system, the inner-loop and outer-loop design is carried out. At the end, the problem of control allocation is solved to transfer the 24 virtual inputs into aerodynamic surface deflections as well as thrust (50 real inputs).

5.1 Inner-Loop Design

The design of the inner-loop flight control law is carried out by using eigenstructure assignment. The eigenvectors of the theoretical rigid-body aircraft with high elastic moments at the joint (cf. Sec.4.1) are used as design goal for the eigenstructure assignment. Since the frequencies of the structural modes are very high, a scaling of the eigenvalues is carried out to reduce the control effort. The designed inner loop separates the formation modes from the rigid-body modes and transforms the highly flexible aircraft formation into a quasi rigid-body aircraft. Fig. 11 shows the closed-loop eigenvalues of the multibody aircraft's flight dynamics and inner loop. With this, stability of the plant is established and the very flexible becomes a flight dynamic structure that is similar to that one of a conventional aircraft. This allows maneuvers like turn or climb and descent that are impossible for the uncontrolled multibody aircraft without elastic moment at the joint. Details to the inner-loop control law design are provided in a related publication [36].

5.2 Outer-Loop Design and Solving the Control Allocation Problem

With the designed inner loops, the aircraft behaves like a conventional rigid-body aircraft. This allows the application of classical flight control concepts. For attitude and airspeed control

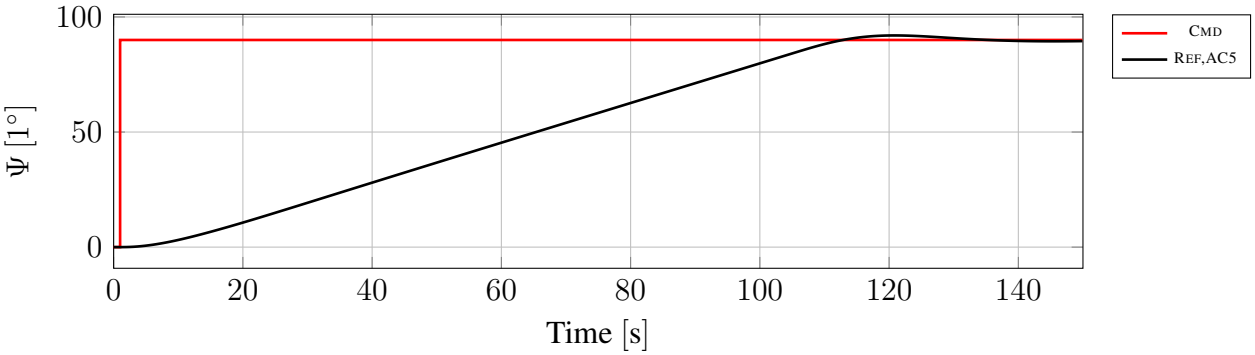

Figure 12: Non-linear response of the azimuth in case of an azimuth step input

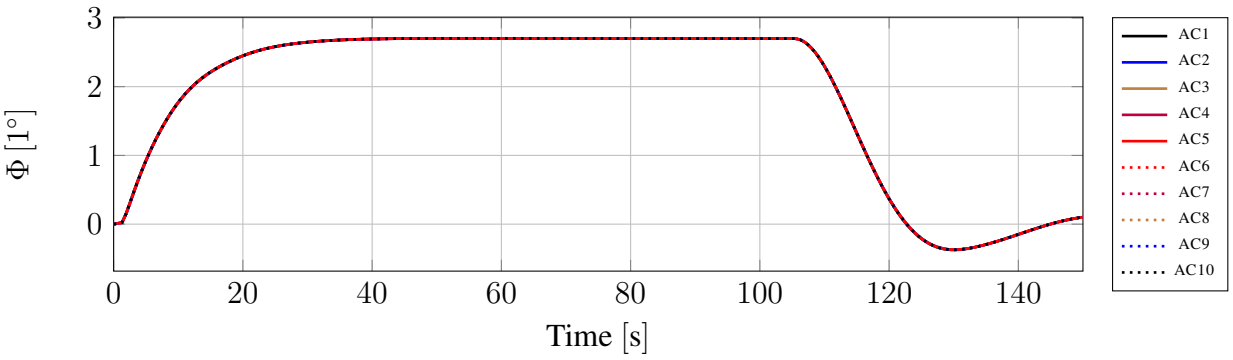

Figure 13: Non-linear response of all bank angles in case of an azimuth step input

a common controller, designed with loop shaping in the frequency domain, is used. Since formation and rigid-body modes are separated from each other, the change in the pitch rate shall be the same for all aircraft within the formation. This can be established by using a generalized pitch rate derivative for all pitch rate derivatives in the virtual control input. The same approach is used for the bank angle control law. Now, a generalized roll rate derivative is used as a common input for all virtual inputs of the roll rate derivatives. For airspeed control, the generalized speed derivative is used as input.

The designed control laws directly command values for the virtual inputs, while the outer loop for altitude and heading control commands desired pitch and bank angle to the attitude control law. Therefore, the control allocation problem is solved for the inner loops as well as attitude and airspeed controller. A frequently used solution for the control allocation is the Moore-Pensorse pseudo-inverse [37]. For the reference test case, the boundaries of the real inputs are violated with this method. Thus, another approach is used. A numerical optimization is carried out to solve the control allocation problem. Using the non-linear model would lead to a high computational effort. Therefore, the linear model of the controlled multibody aircraft is used with step inputs in the bank angle, pitch angle and for the DARPA gust. The optimization is carried out with the toolbox MOPS (*Multi-Objective Parameter Synthesis*) of the German Aerospace Center (DLR) [38]. At the end, a suitable solution for the control allocation problem is found.

The control laws for attitude and azimuth control are designed by simple proportional gains with

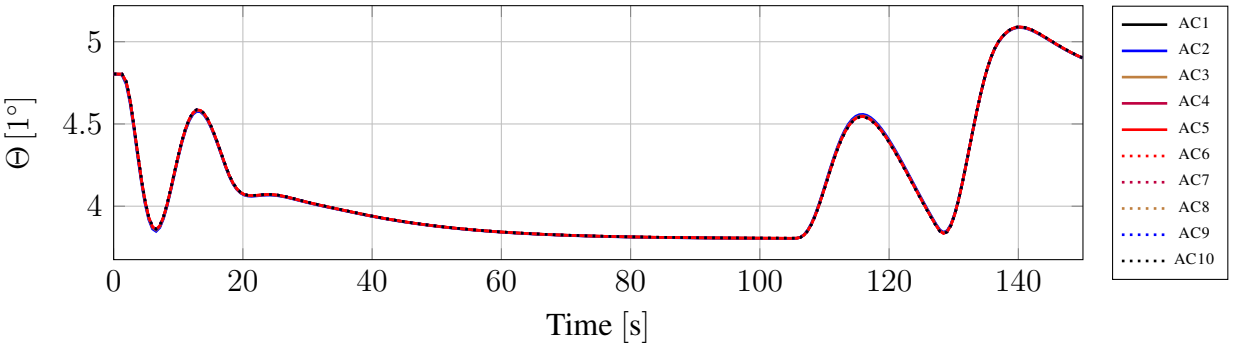

Figure 14: Non-linear response of all pitch angles in case of an azimuth step input

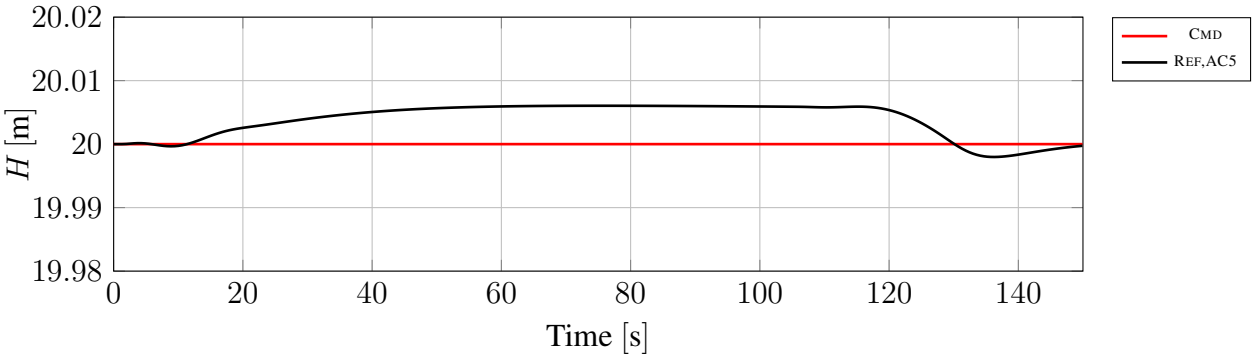

Figure 15: Non-linear response of the altitude in case of an azimuth step input

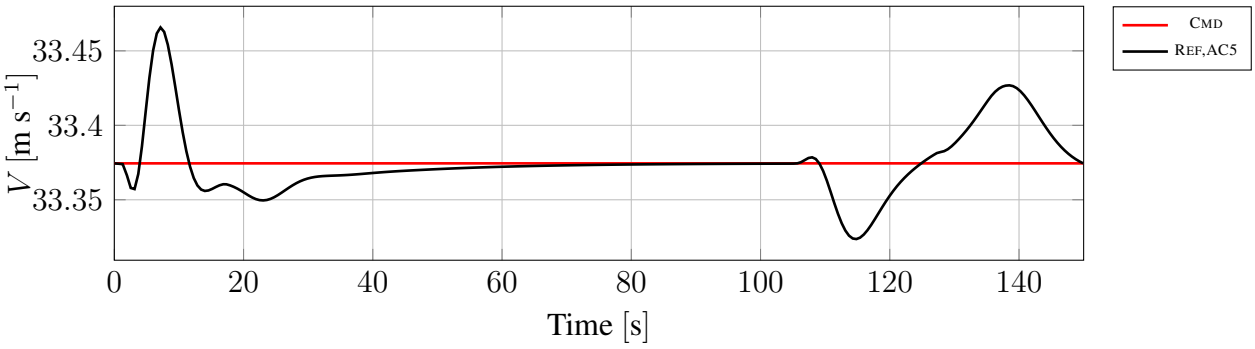

Figure 16: Non-linear response of airspeed in case of an azimuth step input

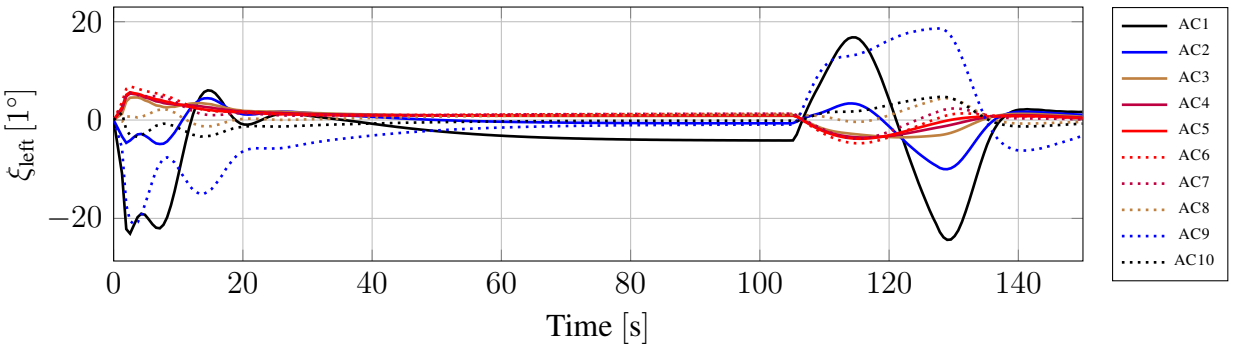

Figure 17: Non-linear response of all left ailerons in case of an azimuth step input

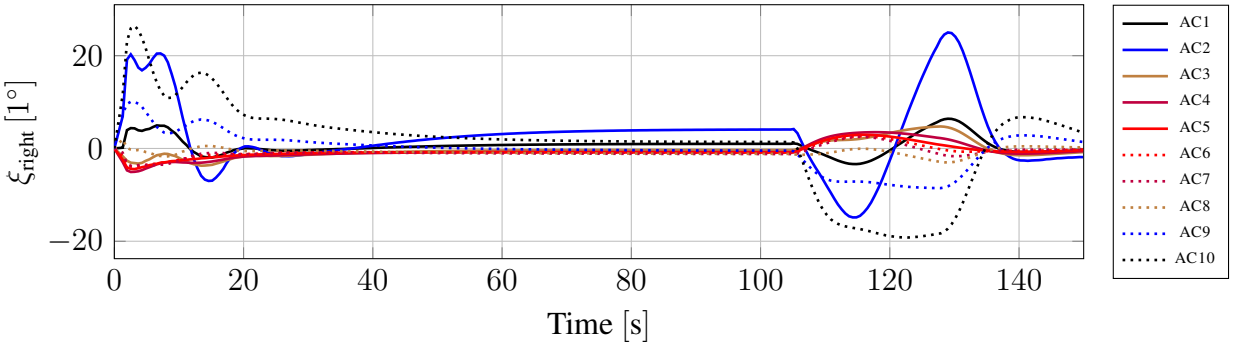

Figure 18: Non-linear response of all right ailerons in case of an azimuth step input

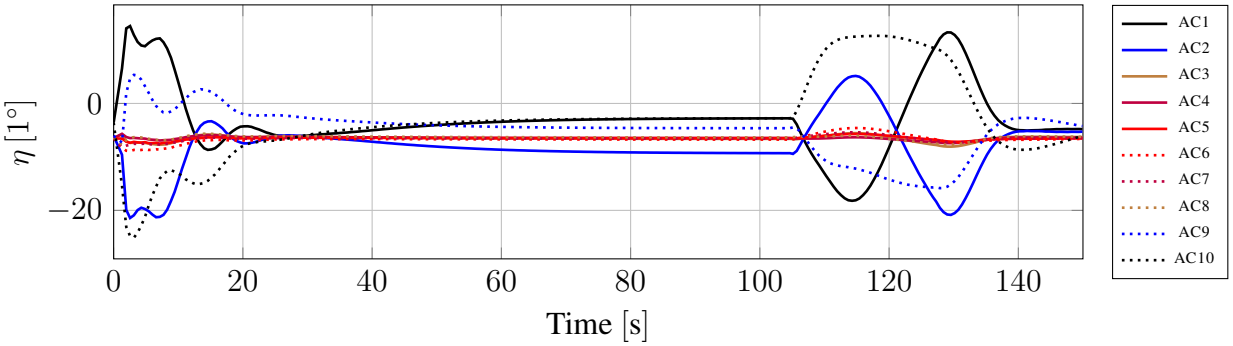

Figure 19: Non-linear response of all elevators in case of an azimuth step input

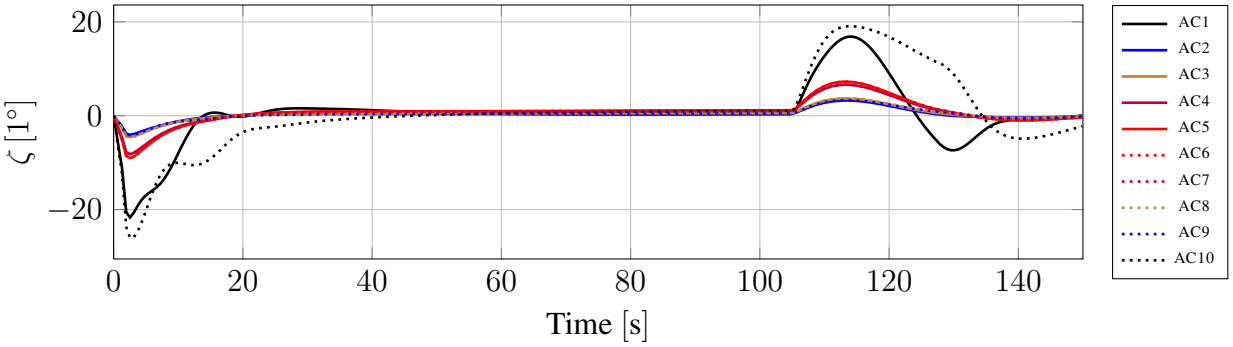

Figure 20: Non-linear response of all rudders in case of an azimuth step input

(a) Flight test with an experimental multibody aircraft shortly after lift-off

(b) Experimental multibody aircraft for further practical investigations

Figure 21: Experimental multibody aircraft configurations

respect to gain and phase margin. In addition, the maximum commanded values of pitch ($\pm 1^\circ$ in relation to the trimmed values) and bank angle ($\pm 2.98^\circ$) are bounded to avoid stall. Fig. 12 to Fig. 20 show non-linear simulation results for a change in the commanded azimuth angle of 90°. A maximum overshoot of 1.97° occurs in the azimuth and the maximum overshoot in the altitude is 6.05 m. Now, differences in the pitch and bank angles of the separate aircraft can be detected. Airspeed control is established with high accuracy. Control surface deflections are within the limits. In summary, a loiter maneuver of the multibody aircraft, which is a typical mission of a HAPS, is suitable with the designed control laws. More details and results to the outer-loop design can be found in a related publication [39].

6 CONCLUSION AND OUTLOOK

This paper summarizes the research activities for multibody aircraft at TU Berlin's department of flight mechanics, flight control and aeroelasticity in the project AlphaLink. It was shown that a multibody aircraft approach is a suitable concept for HAPS with high payload and long endurance. The flight performance allows the fulfilment of the DARPA Vulture program requirements in terms of payload, payload power consumption, operation latitude and endurance. This is achieved through the joint technology that does not transmit bending moments from one aircraft to another one allowing a reduction of the structural weight. A multibody aircraft is a very flexible aircraft configuration that strongly differs from conventional aircraft. The flight dynamics show a strong interference between classical, flight dynamic rigid-body modes and formation modes that are caused by the joint connection between the aircraft. Using hypothetical spring and damping elements at the joint transforms the highly flexible aircraft into a system similar to a rigid-body aircraft. The resulting eigenvector and scaled eigenvalues originate in an artificial, but physically correctly motivated model and are successfully applied to the design of the inner loops using eigenstructure assignment. A clear definition of the design goals becomes possible, providing an advantage in comparison to other methods like the loop shaping or the linear quadratic regulator. Using this approach, the classical cascade flight control law structure for attitude and airspeed control and guidance can be applied to multibody aircraft as well.

In addition to the theoretical investigations, a first flight test was conducted. Fig. 21(a) shows this first flight test at Strausberg airfield, Germany, in 2017. The basic functionality of the innerloops was demonstrated in this flight test. In the future, reproducible experiments will be carried out with an aircraft that is shown in Fig. 21(b). Further research projects will investigate the coupling and decoupling process in flight.

7 References

[1] Maine, K., Devieux, C., and Swan, P. (1995). Overview of iridium satellite network. In *WESCON/'95. Conference record.'Microelectronics Communications Technology Producing Quality Products Mobile and Portable Power Emerging Technologies'*. IEEE.

[2] Botti, J. (2016). Airbus group: A story of continuous innovation. *The Aeronautical Journal*, 120(1223).

[3] Airbus Defence and Space (2018). Airbus zephyr solar high altitude pseudo-satellite flies for longer than any other aircraft during its successful maiden flight.

[4] Newcome, L. (2004). *Unmanned Aviation: A Brief History of Unmanned Aerial Vehicles*. General Publication S. American Institute of Aeronautics and Astronautics.

[5] Završnik, A. (2015). *Drones and Unmanned Aerial Systems: Legal and Social Implications for Security and Surveillance*. Springer.

[6] Noll, T. E., Brown, J. M., Perez-Davis, M. E., et al. (2004). Investigation of the Helios Prototype Aircraft Mishap. Volume I. Mishap Report. *National Aeronautics and Space Administration*, 9.

[7] Su, W. and S. Cesnik, C. E. (2011). Dynamic response of highly flexible flying wings. *AIAA journal*, 49(2).

[8] Lockett, B. (2013). *Flying Aircraft Carriers of the USAF: Wing Tip Coupling*. Lockett-Books.

[9] Vogt, R. (1964). Automatic alignment mechanism for composite aircraft. US Patent 3,161,373.

[10] Shanks, R. E. and Grana, D. C. (1949). Flight tests of a model having self-supporting fuel-carrying panels hinged to the wing tips. *NACA RM L9I07a*.

[11] Bennett, C. V. and Cadman, R. B. (1951). Free-flight-tunnel investigation of the dynamic lateral stability and control characteristics of a tip-to-tip bomber-fighter coupled airplane configuration. *NACA RM L51A12*.

[12] Bennett, C. V. and Boisseau, P. C. (1952). Free-flight-tunnel investigation of the dynamic lateral stability and control characteristics of a high-aspect-ratio bomber model with a sweptback-wing fighter model attached to each wing tip. *NACA RM L52E08*.

[13] Thompson, R. F. (1956). Simulated flight investigation of scaled-speed elastic swept-wing bomber and fighter models coupled wing tip to wing tip. *NACA RM L55J24*.

[14] Diederich, F. W. and Zlotnick, M. (1950). Calculated lift distributions of a consolidated vultee b-36 and two boeing b-47 airplanes coupled at the wing tips. *NACA RM L50I26*.

[15] Holland Jr., R. P. (1966). Air train. US Patent 3,249,322.

[16] Gomez, M. L., Parks, R., and Woodworth, A. J. (2011). Wing tip docking system for aircraft. US Patent 8,061,646.

[17] Magill, S. (2003). Compound aircraft transport study: Wingtip-docking compared to formation flight. In *41st Aerospace Sciences Meeting and Exhibit*.

[18] Morrisey, B. and McDonald, R. (2009). Multidisciplinary design optimization of an extreme aspect ratio hale uav. In *9th AIAA Aviation Technology, Integration, and Operations Conference (ATIO) and Aircraft Noise and Emissions Reduction Symposium (ANERS)*.

[19] Montalvo, C. (2014). *Meta aircraft flight dynamics and controls*. Ph.D. thesis, Georgia Institute of Technology.

[20] Bevilaqua, P. and Tait, P. (2003). Aircraft ferying system and method thereof. US Patent 6,641,082.

[21] Sommer, G. S. (2016). Modular articulated-wing aircraft. US Patent 9,387,926.

[22] Carithers, C. and Montalvo, C. (2018). Experimental control of two connected fixed wing aircraft. *Aerospace*, 5(4), 113.

[23] Cooper, J. R. and Rothhaar, P. M. (2018). Dynamics and control of in-flight wing tip docking. *Journal of Guidance, Control, and Dynamics*, 41(11), 2327–2337.

[24] Behrens, A., Grund, T., Ebert, C., et al. (2018). Investigation of the influence of two wings coupling at their wing tips. *Deutscher Luft- und Raumfahrtkongress*.

[25] Wright, J. R. and Cooper, J. E. (2008). *Introduction to aircraft aeroelasticity and loads*, vol. 20. John Wiley & Sons.

[26] Kane, T. R. and Levinson, D. A. (1985). *Dynamics, theory and applications*. McGraw Hill.

[27] Katz, J. and Plotkin, A. (2001). *Low-Speed Aerodynamics*. Cambridge University Press.

[28] Marsh, G. (2010). Best endurance under the sun. *Renewable Energy Focus*, 11(5).

[29] Defense Advanced Research Program Agency (2007). Vulture program. *Broad Agency Announcement (BAA) Solicitation 07-51*.

[30] Raymer, D. P. (2006). *Aircraft design: a conceptual approach and Rds-student, software for aircraft design, sizing, and performance set (AIAA Education)*. AIAA (American Institute of Aeronautics & Astronautics).

[31] Roskam, J. (1985). *Airplane design*. Roskam Aviation and Engineering Corp.

[32] Torenbeek, E. (2013). *Synthesis of subsonic airplane design: an introduction to the preliminary design of subsonic general aviation and transport aircraft, with emphasis on layout, aerodynamic design, propulsion and performance*. Springer.

[33] Sóbester, A., Keane, A., Scanlan, J., et al. (2005). Conceptual design of uav airframes using a generic geometry service. In *Infotech@ Aerospace*.

[34] Obert, E. (2009). *Aerodynamic design of transport aircraft*. IOS Press.

[35] Phillips, W. F., Fugal, S. R., and Spall, R. E. (2006). Minimizing induced drag with wing twist, computational-fluid-dynamics validation. *Journal of Aircraft*, 43(2).

[36] Köthe, A. and Luckner, R. (2019). Applying eigenstructure assignment to inner-loop flight control laws for a multibody aircraft. In *5th CEAS Conference on Guidance, Navigation and Control*.

[37] Durham, W., Bordignon, K. A., and Beck, R. (2017). *Aircraft control allocation*. John Wiley & Sons.

[38] Joos, H.-D. (1997). Multi-objective parameter synthesis (MOPS). In *Robust Flight Control*. Springer, pp. 199–217.

[39] Köthe, A. and Luckner, R. (2019). Outer-loop control law design with control allocation for a multibody aircraft. In *5th CEAS Conference on Guidance, Navigation and Control*.

COPYRIGHT STATEMENT

The authors confirm that they, and/or their company or organization, hold copyright on all of the original material included in this paper. The authors also confirm that they have obtained permission, from the copyright holder of any third party material included in this paper, to publish it as part of their paper. The authors confirm that they give permission, or have obtained permission from the copyright holder of this paper, for the publication and distribution of this paper as part of the IFASD-2019 proceedings or as individual off-prints from the proceedings.